Self Energy effect in frequency dependent Vertex flow equation

D. Vilardi, C. Taranto, and W. Metzner
Max Planck Institute for Solid State Research, Stuttgart
(Dated: July 25, 2017)

blablabl ...

PACS numbers:

I. INTRODUCTION

- Much of the weak coupling momentum structure of the vertex (for the fermionic Hubbard model) is know by means of fRG,its frequency structure has been investigated much less.

- In recent years several results have been obtained for the single impurity Anderson model vertex, both on its own and as essential ingredient for diagrammatic extensions of DMFT. Citare: Rohringer, Kinza, Hafermann, Karrasch, Wentzell (and references therein) for the SIAM. Extensions of DMFT: DGA, DF, DMF2RG, Trilex, Quadrilex.

- A systematic study keeping into account the full frequency dependence and a physically motivated approximation for the momentum dependence, and including fluctuations in all channels is still lacking.

- Our results show the feasibility, and, in some respects, the necessity of a complete treatment of the frequency dependence of the vertex, whose impact is particularly large in methods that aim at strong coupling.

- We will confirm some results already foreseen by 1, who has shown a "forward scattering instability" already with a simpler frequency parametrization.

- With the study of the frequency dependence of the vertex we understand the appearance of a *scattering instability.*

- The d-wave superconductivity is reduced.

- The frequency dependent vertex allows to compute a frequency dependent self energy, often neglected in static fRG.

- We will show that the self-energy feedback in the flow equations is essential to guarantee the consistency between vertex and propagators in the flow equations.

- even a Fermi-liquid self-energy can qualitatively change the physical results.

II. FORMALISM

A. Model

The Hubbard model[2] describes spin-$\frac{1}{2}$ fermions with a local interaction:

$$\mathcal{H} = \sum_{i,j,\sigma} t_{ij} c^\dagger_{i,\sigma} c_{j,\sigma} + U \sum_i n_{i,\uparrow} n_{i,\downarrow} \tag{1}$$

where $c^\dagger_{i,\sigma}$ and $c_{i,\sigma}$ are, respectively, creation and annihilation operators for fermions with spin $\sigma =\uparrow,\downarrow$. We consider the two-dimensional case with square lattice and repulsive interaction $U > 0$ at finite temperature T and in the SU(2) spin-symmetric phase. The hopping amplitude is restricted to $t_{ij} = -t$ for nearest neighbors, $t_{ij} = -t'$ for next-to-nearest neighbors. We take $t \equiv 1$ as energy unit. The Fourier transform allow us to write the bare dispersion of the Hubbard hamiltonian:

$$\varepsilon_{\mathbf{k}} = -2t\,(\cos k_x + \cos k_y) - 4t' \cos k_x \cos k_y. \tag{2}$$

B. Flow equations

In the following paragraph we will give some details about the functional renormalization group,[3,4] clarifying the notation used for the vertex.

Generally speaking, the fRG implements the renormalization group idea in the functional integral formalism. This is done by endowing the action with an additional dependence on a scale-parameter Λ:[3,4]

$$\mathcal{S}^\Lambda[\overline{\psi},\psi] = -(\overline{\psi}, {G_0^\Lambda}^{-1}\psi) + \mathcal{S}_{\rm int}, \tag{3}$$

where $\mathcal{S}_{\rm int}$ is the interaction part, and $(\overline{\psi},\psi)$ summarizes the summation over all the quantum numbers of the fermionic fields $\overline{\psi}$ and ψ. The scale dependence, acquired through the non-interacting propagator G_0^Λ, generates flow equations (with known initial conditions) for functional integrals,[5] like the effective action, the effective interaction, or the generating functional for the connected Green's function. The final result is recovered for some final Λ-value so that: $G_0^{\Lambda_{\rm f}} = G_0$, and the original action is restored.

We will apply this approach to the effective action, whose expansions in the fields generates the one-particle irreducible (1PI) functions. By expanding the functional

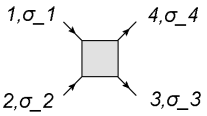

Figure 1: Notation of the two-particle vertex. **placeholder**

flow equation, one obtains a hierarchy of flow equations for the 1PI functions, involving vertices of arbitrarily high orders. We will restrict ourselves to the two-particle level truncation by retaining only the two lowest nonvanishing orders in the expansion, i.e., we consider the flow of the self-energy Σ^Λ and of the two-particle vertex V^Λ, neglecting the effects of higher order vertices. This truncation restricts the applicability of the approach to the weak-to-moderate coupling regime[6]. It can be further shown that, at the two-particle level trunctaion, the fRG sums up efficiently, although approximately, the so-called parquet-diagrams[7–9].

Due to translational invariance, we can use the energy and momentum conservation to fix one of the arguments of the self-energy and of the vertex. Due to SU(2) symmetry, the self-energy is diagonal in spin-space:

$$\Sigma^\Lambda_{\sigma\sigma'}(k) = \Sigma(k)\delta_{\sigma,\sigma'}, \tag{4}$$

where $k = (\nu, \mathbf{k})$, ν is a fermionic Matsubara frequency and $\mathbf{k}$ a momentum in the first Brillouin zone.

For the notation of the two-particle vertex function $V_{\sigma_1\sigma_2\sigma_3\sigma_4}(k_1, k_2, k_3)$ we refer to Fig. 1, where $k_i = (\nu_i, \mathbf{k_i})$. The momentum $k_4 = k_1 + k_2 - k_3$ is fixed by conservation.Furthermore SU(2)-symmetry guarantees that the vertex does not vanish only for six spin combinations: $V^\Lambda_{\uparrow\uparrow\uparrow\uparrow} = V^\Lambda_{\downarrow\downarrow\downarrow\downarrow}$, $V^\Lambda_{\uparrow\downarrow\uparrow\downarrow} = V^\Lambda_{\downarrow\uparrow\downarrow\uparrow}$, and $V^\Lambda_{\uparrow\downarrow\downarrow\uparrow} = V^\Lambda_{\downarrow\uparrow\uparrow\downarrow}$. Finally, due to SU(2) symmetry and crossing relation one has:[10]

$$\begin{aligned} V^\Lambda_{\uparrow\uparrow\uparrow\uparrow}(k_1,k_2,k_3) &= V^\Lambda_{\uparrow\downarrow\uparrow\downarrow}(k_1,k_2,k_3) \\ &\quad - V^\Lambda_{\uparrow\downarrow\uparrow\downarrow}(k_1,k_2,k_1+k_2-k_3), \quad (5) \\ V^\Lambda_{\uparrow\downarrow\downarrow\uparrow}(k_1,k_2,k_3) &= -V^\Lambda_{\uparrow\downarrow\uparrow\downarrow}(k_1,k_2,k_1+k_2-k_3). \quad (6) \end{aligned}$$

This allows us to consider only one function of three arguments for the vertex: $V^\Lambda(k_1,k_2,k_3) \equiv V^\Lambda_{\uparrow\downarrow\uparrow\downarrow}(k_1,k_2,k_3)$, all the others spin components being obtained by Eqs. (4-5)[11].

With these considerations the flow equation for the self energy[3] reads:

$$\frac{d}{d\Lambda}\Sigma^\Lambda(k) = -\int_p S^\Lambda(p)\left[2V^\Lambda(k,p,p) - V^\Lambda(k,p,k)\right], \tag{7}$$

with $p = (\omega, \mathbf{p})$ and $k = (\nu, \mathbf{k})$. We use the notation $\int_p = T\sum_\omega \int_{\mathbf{p}}$ with $\int_{\mathbf{q}} = \int \frac{d\mathbf{q}}{4\pi^2}$ being the normalized integral over the first Brillouin zone.

$$S^\Lambda = \left.\frac{dG^\Lambda}{d\Lambda}\right|_{\Sigma^\Lambda=\text{const}} \tag{8}$$

is the single-scale propagator and $G^\Lambda = \left[(G_0^\Lambda)^{-1} - \Sigma^\Lambda\right]^{-1}$ is the full propagator.

The vertex flow equation[3,11] can be written as:

$$\frac{d}{d\Lambda}V^\Lambda(k_1,k_2,k_3) = \mathcal{T}^\Lambda_{\text{pp}}(k_1,k_2,k_3) + \mathcal{T}^\Lambda_{\text{ph}}(k_1,k_2,k_3) + \mathcal{T}^\Lambda_{\text{phc}}(k_1,k_2,k_3), \tag{9}$$

where:[23]

$$\begin{aligned} \mathcal{T}^\Lambda_{\text{pp}}(k_1,k_2,k_3) &= -\frac{1}{2}\int_p \mathcal{P}^\Lambda(p,k_1+k_2-p)\Big\{V^\Lambda(k_1,k_2,k_1+k_2-p)V^\Lambda(k_1+k_2-p,p,k_3) \quad (10) \\ &\quad + V^\Lambda(k_1,k_2,p)V^\Lambda(p,k_1+k_2-p,k_3)\Big\}; \\ \mathcal{T}^\Lambda_{\text{ph}}(k_1,k_2,k_3) &= -\int_p \mathcal{P}^\Lambda(p,k_3-k_1+p)\Big\{2V^\Lambda(k_1,k_3-k_1+p,k_3)V^\Lambda(p,k_2,k_3-k_1+p) \quad (11) \\ &\quad - V^\Lambda(k_1,k_3-k_1+p,p)V^\Lambda(p,k_2,k_3-k_1+p) - V^\Lambda(k_1,k_3-k_1+p,k_3)V^\Lambda(k_2,p,k_3-k_1+p)\Big\}; \\ \mathcal{T}^\Lambda_{\text{phc}}(k_1,k_2,k_3) &= \int_p \mathcal{P}^\Lambda(p,k_2-k_3+p)V^\Lambda(k_1,k_2-k_3+p,p)V^\Lambda(p,k_2,k_3). \quad (12) \end{aligned}$$

Here we have defined the quantity:

$$\mathcal{P}^\Lambda(p,Q+p) = G^\Lambda(p)S^\Lambda(Q+p) + G^\Lambda(p+Q)S^\Lambda(p), \tag{13}$$

which is the scale-derivative, at fixed self energy, of a Green's function bubble with frequency and momentum transfer Q.

III. VERTEX APPROXIMATION

In order to deal with the frequency and momentum dependence of the vertex, we start by decomposing it as follows:

$$V^{\Lambda}(k_1,k_2,k_3) = U - \phi_{\rm p}^{\Lambda}(k_1+k_2;k_1,k_3) + \phi_{\rm m}^{\Lambda}(k_3-k_1;k_1,k_2) + \frac{1}{2}\phi_{\rm m}^{\Lambda}(k_2-k_3;k_1,k_2) - \frac{1}{2}\phi_{\rm c}^{\Lambda}(k_2-k_3;k_1,k_2), \quad (14)$$

where we introduced the pairing channel $\phi_{\rm p}$, the magnetic channel $\phi_{\rm m}$ and the charge channel $\phi_{\rm c}$. Substituting Eq. (13) in Eq. (8) we obtain:

$$-\dot{\phi}_{\rm p}^{\Lambda}(k_1+k_2;k_1,k_3) + \dot{\phi}_{\rm m}^{\Lambda}(k_3-k_1;k_1,k_2) + \frac{1}{2}\dot{\phi}_{\rm m}^{\Lambda}(k_2-k_3;k_1,k_2) - \frac{1}{2}\dot{\phi}_{\rm c}^{\Lambda}(k_2-k_3;k_1,k_2) = \mathcal{T}_{\rm pp}^{\Lambda}(k_1,k_2,k_3) + \mathcal{T}_{\rm ph}^{\Lambda}(k_1,k_2,k_3) + \mathcal{T}_{\rm phc}^{\Lambda}(k_1,k_2,k_3). \quad (15)$$

We associate the momentum transfer argument of $\mathcal{P}^{\Lambda}$ in Eqns. (9-11) to the momentum transfer argument of the $\phi_{\rm x}$ on the right hand side of Eq. 13. This way, it is easy to attribute $\mathcal{T}_{\rm pp}^{\Lambda}$ to the flow equation of the only function in Eq. (14) that depends explicitly on k_1+k_2: $-\dot{\phi}_{\rm p}^{\Lambda} = \mathcal{T}_{\rm pp}^{\Lambda}$. The same is true for the particle hole crossed channel: $\mathcal{T}_{\rm phc}^{\Lambda} = \dot{\phi}_{\rm m}^{\Lambda}$. We associate to the particle-hole diagram the third and fourth term on the left hand side of Eq. (14): $\mathcal{T}_{\rm ph}^{\Lambda}(k_1,k_2,k_3) = \frac{1}{2}\dot{\phi}_{\rm m}^{\Lambda}(k_2-k_3;k_1,k_2) - \frac{1}{2}\dot{\phi}_{\rm c}^{\Lambda}(k_2-k_3;k_1,k_2)$. Hence the flow equations for ϕ then read:

$$\dot{\phi}_{\rm p}^{\Lambda}(Q;k_1,k_3) = -\mathcal{T}_{\rm pp}^{\Lambda}(k_1,Q-k_1,k_3), \quad (16)$$

$$\dot{\phi}_{\rm c}^{\Lambda}(Q;k_1,k_2) = -2\mathcal{T}_{\rm ph}^{\Lambda}(k_1,k_2,k_2-Q) + \mathcal{T}_{\rm phc}^{\Lambda}(k_1,k_2,Q+k_1), \quad (17)$$

$$\dot{\phi}_{\rm m}^{\Lambda}(Q;k_1,k_2) = \mathcal{T}_{\rm phc}^{\Lambda}(k_1,k_2,Q+k_1), \quad (18)$$

where $Q=(\Omega,\mathbf{Q})$ is a frequency and momentum transfer.

Following Refs. 1,11, we address first the momentum dependence. To this end, we introduce a decomposition of unity by means of a set of orthonormal form factors for the two fermionic momenta $\{f_l(\mathbf{k})\}$ obeying the completeness relation[12]:

$$\int_{\mathbf{k}} f_l(\mathbf{k}) f_m(\mathbf{k}) = \delta_{l,m}. \quad (19)$$

The procedure outlined here is described in detail, e.g., in Ref. 12.

We can then project each channel on a subset of form factors, whose choice is physically motivated[11]. Let us stress that if one could keep all the form factors the expansion would be exact.

For the pairing channel we keep only $f_s(\mathbf{k}) = 1$ and $f_d(\mathbf{k}) = \cos k_x - \cos k_y$:

$$\phi_{\rm p}^{\Lambda}(Q;k_1,k_3) = \mathcal{S}_{\mathbf{Q}}^{\Omega;\nu_1,\nu_3} + f_d\left(\frac{\mathbf{Q}}{2}-\mathbf{k}_1\right) f_d\left(\frac{\mathbf{Q}}{2}-\mathbf{k}_3\right) \mathcal{D}_{\mathbf{Q}}^{\Omega;\nu_1,\nu_3}. \quad (20)$$

The divergence in the channel $\mathcal{S}$ is associated to the emergence of s-wave superconductivity, while $\mathcal{D}$ to d-wave superconductivity.[3,4]

For the charge and magnetic channels we restrict ourselves to $f_s(\mathbf{k}) = 1$ only:

$$\phi_{\rm c}^{\Lambda}(Q;k_1,k_2) = \mathcal{C}_{\mathbf{Q}}^{\Omega;\nu_1,\nu_2}, \quad (21)$$

$$\phi_{\rm m}^{\Lambda}(Q;k_1,k_2) = \mathcal{M}_{\mathbf{Q}}^{\Omega;\nu_1,\nu_2}, \quad (22)$$

corresponding to instabilities in the charge and magnetic channels, respectively (for notation simplicity we omit the Λ-dependencies of the channel functions $\mathcal{S}$, $\mathcal{D}$, $\mathcal{C}$ and $\mathcal{M}$).

Let us stress that for each channel in Eq. (13) we have defined *its own* frequency notation, consisting of one transfer frequency in the specific channel and two remaining independent fermionic frequencies. At finite temperature the frequency transfer is a bosonic Matsubara frequency.

The choice of the mixed notation is the most natural? since the transferred momentum and frequency play a special role in the diagrammatics. Indeed, it is the only dependence generated in second order perturbation theory and the main dependence in finite order perturbation theory. This notation is also convenient to express the Bethe-Salpeter equations[10], which are deeply related to parquet-approximations and fRG.

Although one expects a leading dependence in the bosonic frequency, in particular in the weak coupling regime, we will see that in some cases the dependence on fermionic frequencies can become strong and not negligible.

In Refs. 11, with a simplified frequency dependence, the channel functions above are interpreted as bosonic exchange propagators. Such an interpretation is missing with full frequency-dependence.

The flow equations for the channels $\mathcal{S}$, $\mathcal{D}$, $\mathcal{C}$ and $\mathcal{M}$ can be derived from the projection onto form factors of

Eq. (9)-(11):

$$\dot{\mathcal{S}}_{\mathbf{Q}}^{\Omega;\nu_1,\nu_3} = -\int_{\mathbf{k}_1,\mathbf{k}_3} \mathcal{T}_{\rm pp}(k_1, Q-k_1, k_3); \quad (23)$$

$$\dot{\mathcal{D}}_{\mathbf{Q}}^{\Omega;\nu_1,\nu_3} = -\int_{\mathbf{k}_1,\mathbf{k}_3} f_d\left(\frac{\mathbf{Q}}{2}-\mathbf{k}_1\right) f_d\left(\frac{\mathbf{Q}}{2}-\mathbf{k}_3\right) \mathcal{T}_{\rm pp}(k_1, Q-k_1, k_3); \quad (24)$$

$$\dot{\mathcal{C}}_{\mathbf{Q}}^{\Omega;\nu_1,\nu_2} = \int_{\mathbf{k}_1,\mathbf{k}_2} \mathcal{T}_{\rm phc}(k_1, k_2, Q+k_1) - 2\mathcal{T}_{\rm ph}(k_1, k_2, k_2-Q); \quad (25)$$

$$\dot{\mathcal{M}}_{\mathbf{Q}}^{\Omega;\nu_1,\nu_2} = \int_{\mathbf{k}_1,\mathbf{k}_2} \mathcal{T}_{\rm phc}(k_1, k_2, Q+k_1). \quad (26)$$

The final equations are then obtained by substituting the decomposition (13) into the equations above, and using trigonometric equalities. As an example we report here the equation for the magnetic channel, while the expression for the other channels are reported in the Appendix:

$$\dot{\mathcal{M}}_{\mathbf{Q}}^{\Omega;\nu_1,\nu_2} = \sum_{\nu} L_{\rm m\,\mathbf{Q}}^{\Omega;\nu_1,\nu} P_{\mathbf{Q}}^{\Omega,\nu} L_{\rm m\,\mathbf{Q}}^{\Omega;\nu,\nu_2-\Omega}, \quad (27)$$

with:

$$P_{\mathbf{Q}}^{\Omega;\omega} = \int_{\mathbf{p}} G^{\Lambda}_{\mathbf{p},\omega} S^{\Lambda}_{\mathbf{Q}+\mathbf{p},\Omega+\omega} + G^{\Lambda}_{\mathbf{Q}+\mathbf{p},\Omega+\omega} S^{\Lambda}_{\mathbf{p},\omega}, \quad (28)$$

and:

$$\begin{aligned} L_{\rm m\,\mathbf{Q}}^{\Omega;\nu_1,\nu_2} &= U + \mathcal{M}_{\mathbf{Q}}^{\Omega;\nu_1,\nu_2} \\ &+ \int_{\mathbf{p}} \Big\{ -\mathcal{S}_{\mathbf{p}}^{\nu_1+\nu_2;\nu_1,\nu_1+\Omega} \\ &-\tfrac{1}{2}\ \mathcal{D}_{\mathbf{p}}^{\nu_1+\nu_2;\nu_1,\nu_1+\Omega}[\cos(Q_x)+\cos(Q_y)] \\ &+\tfrac{1}{2}\ \left[\mathcal{M}_{\mathbf{p}}^{\nu_2-\nu_1-\Omega;\nu_1,\nu_2} - \mathcal{C}_{\mathbf{p}}^{\nu_2-\nu_1-\Omega,\nu_1,\nu_2}\right]\Big\} \end{aligned} \quad (29)$$

Note that after the momentum integrals in P and L are performed, the right hand side can be expressed as a matrix-matrix multiplication in frequency space, where Ω and $\mathbf{Q}$ appear as parameters.

After this decomposition, the evaluation of the vertex-flow equation, depending on six arguments, is reduced to the flow of the four functions $\mathcal{S}$, $\mathcal{D}$, $\mathcal{C}$, $\mathcal{M}$ each of them depending on three frequencies and one momentum only. In order to compute these equations numerically we discretize the momentum dependence on patches covering the Brillouin zone and truncate the frequency dependence to some maximal frequency value. More details about this are given in the Appendix.

Let us stress that, while the form-factor projection procedure is well defined in momentum space, a similar approximation for the frequency, i.e., reducing the vertex frequency dependence to a frequency transfer only[1,14,15], is more problematic. Indeed this projection in frequency space requires that the two remaining frequencies are chosen arbitrarily. This choice affects quantitatively and qualitatively the results, for reasons that are clear looking at the frequency structure of the vertex, discussed below.

A. Cutoff scheme

To use the flow equations defined above we need to specify the Λ-dependence of the non interacting propagator G_0^{Λ}, often referred to as *cutoff scheme*, in connection to the scale-separation of the renormalization group. We have used two different cutoffs.

For most our calculations we have used the *interaction cutoff*, introduced in Ref. 16:

$$G_0^{\Lambda}(k) = \Lambda G_0(k) = \frac{\Lambda}{i\nu + \mu - \varepsilon_{\mathbf{k}}}, \quad (30)$$

Where the scale-parameter Λ flows from 0 to 1. μ is the chemical potential needed to fix the occupation at the desired value n. Correspondingly the interacting Green's function reads:

$$G^{\Lambda}(k) = \frac{\Lambda}{i\nu - \varepsilon_{\mathbf{k}} + \mu^{\Lambda} - \Lambda\Sigma^{\Lambda}(k)} \quad (31)$$

We have introduced a Λ-dependent chemical potential to maintain the occupation fixed during the flow. The chemical potential becomes a functional of the flowing self-energy, $\mu = \mu[\Sigma^{\Lambda}]$, whose value is found by solving the equation:

$$n = n^{\Lambda}(\mu) \equiv \int_k \frac{e^{i\nu 0^+}}{i\nu - \varepsilon_{\mathbf{k}} + \mu^{\Lambda} - \Lambda\Sigma^{\Lambda}(k)}. \quad (32)$$

for μ.

The main advantage of the interaction cutoff is that the Λ-dependent action can be interpreted[16] as the physical action of the system with rescaled interaction $\tilde{U}^{\Lambda} = \Lambda^2 U$.

Since T acts as an infrared cutoff, for our purposes we do not need to worry about the fact that this cutoff is not scale-selective, and hence does not regularize possible divergences in the bubbles. Furthermore it has been shown in Ref. 17 that, in the context of the single-impurity Anderson model, the vertex-structures do not depend qualitatively on the cutoff-choice, and the specific effect of the interaction-cutoff on the vertex frequency structure has been studied in detail.

As a benchmark for the robustness of our results on the cutoff-choice, we have used a soft version of the *frequency selective cutoff* defined[18] by:

$$G_0^{\Lambda}(k) = \frac{1}{i\,\mathrm{sign}\sqrt{\nu^2+\Lambda^2} - \mu - \varepsilon_{\mathbf{k}}}, \quad (33)$$

with $\Lambda_0 = \infty$ and $\Lambda_{\rm f} = 0$. Also in this case we have performed our calculations at fixed occupation.

For both our cutoff choices at the beginning of the flow one has $G_0^{\Lambda_0} = 0$, corresponding to a initial conditions for the self-energy and the vertex defined by, $\Sigma^{\Lambda_0} = 0$ and $V^{\Lambda_0} = U$.

IV. RESULTS

In the next section, we present our results obtained by full frequency dependent fRG. All the results are pre-

sented in units of $t = 1$.

Numerical implementation We have implemented numerically the flow equations reported in the appendix. Due to the different nature of the momentum arguments of self-energy and vertex we have defined two different patching schemes of the irreducible Brillouin zone. Similarly to what is done in Ref. 11, the vertex patching describes more accurately the corners around $(0, 0)$ and (π, π), where we expect the instability vectors.

The situation is completely different for the self-energy, for which the most relevant physics happens in the vicinity of the Fermi surface. Therefore we concentrate the patches along the Fermi surface and in its immediate vicinity (see Figs. 9 and 10), with more points close to the *antinodal* region near $(\pi, 0)$, relevant for antiferromagnetism.

In the calculations presented in the following we have used 29 patches for the vertex and 44 for the self-energy.

For the practical implementation of the frequency dependence we found convenient to rewrite $\mathcal{S}$, $\mathcal{D}$, $\mathcal{C}$ and $\mathcal{M}$ as functions of three bosonic frequencies. For each frequency argument we restricted ourselves to at least 40 positive and 40 negative Matsubara frequencies. Beyond these frequencies we have used the asymptotical values. We stress that the number of Matsubara frequencies that can be taken into account sets the lowest temperature reachable by the calculation.

A. Analysis of instabilities

By means of fRG one can perform an instability analysis of the system: for some value of the flow parameter Λ one of the channels shows a divergence. The value Λ_c for which this happens is called *critical scale*, and from the diverging channel one can infer the leading instability of the system. In Fig. 2 we show the critical scale $1 - \Lambda_c$ as a function of the doping $x = 1 - n$ with and without self-energy feedback, for $T = 0.08t$, $t' = -0.32t$ and $U = 4t$. We show our result in terms of $1 - \Lambda$, which vanishes at the end of the flow. For the physical interpretation of Λ_c in the interaction flow, we refer to the rescaled interaction[16] $\tilde{U}^\Lambda$ as discussed in Sec.**??**.

We defined the critical scale as the cutoff value for which the value of the largest channel exceeds $200t$. We checked that these results are also consistent with stability analysis based on the susceptibilities.

A divergence of the vertex at finite temperature is associated with a symmetry breaking, in violation of the Mermin-Wagner theorem.[19] This is a consequence of the truncation of the flow equations. Instead, we should interprete the finite temperature vertex divergence as the signal of the appearance of strong bosonic fluctuations that cannot be treated within the approximation-scheme we are using.[6] Even though in our framework the flow cannot be continued beyond the critical scale, from the analysis of vertex and self-energy we can identify the relevant effective interactions of the system.

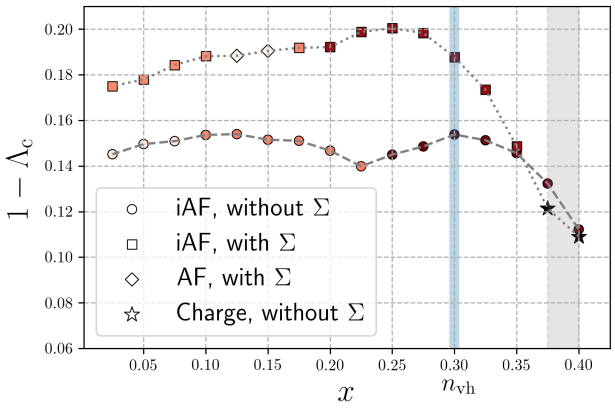

Figure 2: Critical scale $1 - \Lambda_c$ as a function of the doping $x = 1 - n$, for $T = 0.08t$, $t' = -0.32t$ and $U = 4t$. Square symbols and circles refer to incommensurate antiferromagnetism (iAF), respectively without and with self-energy feedback. The black stars refer to a divergence in the charge channel (forward scattering in Ref. 1). The color of squares and circles encodes the distance of the incommensurability vector from (π, π): darker color corresponds to higher incommensurability. The darkest color corresponds to $\delta = 1.13$. The vertical light blue line marks the van Hove filling.

For the parameter sets shown in Fig. 2 and without self-energy feedback (square and star symbols), there are two possible instabilities. For doping smaller than 0.35 the leading fluctations of the system are either commensurate or incommensurate antiferromagnetic. The incommensurability δ is defined through $\mathbf{Q} = (\pi, \pi - \delta)$, the momentum where the magnetic channel $\mathcal{M}^\Lambda$ has its maximum. The region of commensurate antiferromagnetism for $0.125 \leq x \leq 0.150$ has to be attributed to the presence of a large plateau around (π, π) in the bare bubble. Correspondingly the commensurate peak in the susceptibility coexists with incommensurate ones of similar magnitude.

The most striking feature in Fig.2 is the presence of a divergence in the charge channel $\mathcal{C}^\Lambda$ at $\mathbf{Q} = (0, 0)$ for the largest values of doping, marked by black stars. This feature was already observed by Husemann *et al.* in Ref. 11, where it was named *forward scattering instability*. The charge channel $\mathcal{C}^\Lambda$ diverges for finite frequency transfer $\Omega = 2\pi/\beta$, which makes the interpretation of the divergence in terms of a physical instability not obvious. The frequency structure of the charge channel $\mathcal{C}^\Lambda$ together with its origin will be discussed further in paragraph **??**.

The self-energy feedback has three effects, as can be seen from the circular symbols in Fig. 2. First, the self-energy feedback decreases $1 - \Lambda_c$. Second, the incommensurability vector is affected, the region of commensurate antiferromagnetism disappears, and one can observe a more regular trend of increasing δ in terms of x. Third, the divergence in the charge channel is completely suppressed, and the leading instability in the doping region

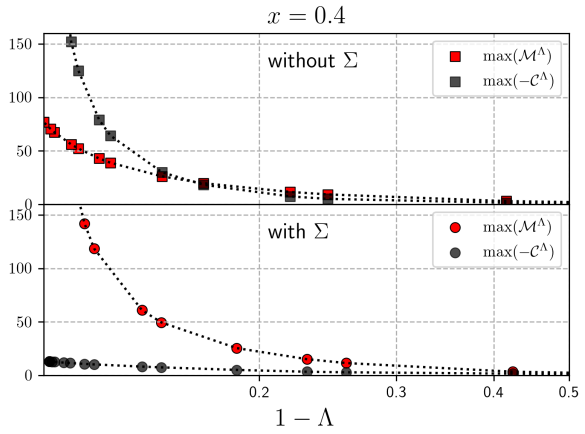

Figure 3: Flow of the maximal value of the charge ($\mathcal{C}$) and magnetic ($\mathcal{M}$) channels as functions of Λ, for $x = 0.4$, $t' = -0.32$, $U = 4t$ and $T = 0.08t$. Top: without self-energy feedback; bottom: with self-energy feedback.

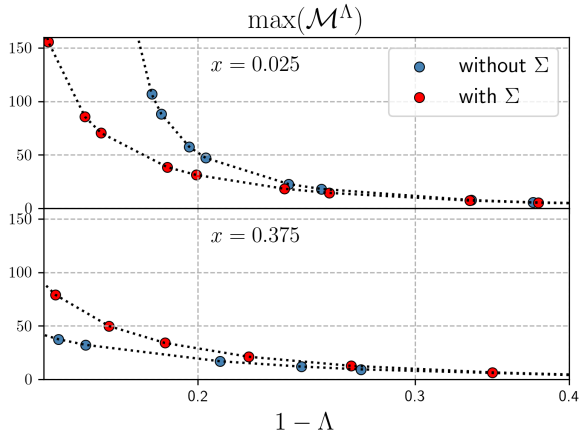

Figure 4: Flow of the maximal value of the magnetic ($\mathcal{M}$) channel as functions of Λ, for $x = 0.025$ (top) and $x = 0.375$ (bottom). The other parameters are $t' = -0.32$, $U = 4t$ and $T = 0.08t$. Red symbols: with self-energy feedback; blue symbols: without self-energy feedback.

$0.375 \leq x \leq 0.4$ remains incommensurate antiferromagnetic. This can be also seen from Fig. 3, where we compare the flow of the maximum (of the absolute value) of magnetic and charge channels with and without the self-energy feedback for doping $x = 0.4$. Without self-energy feedback, the charge channel reaches large and negative values. The presence of such a large (and negative) charge channel inhibits the magnetic channel. The effect of the self-energy in the flow is evident, as can be seen from the bottom inset: the charge channel is strongly damped. At the same time the magnetic channel is enhanced.

This is confirmed by Fig. 4, where we show the maximum of $\mathcal{M}$ with and without self-energy feedback for $x = 0.025$ (top inset) and $x = 0.375$ (bottom inset). One

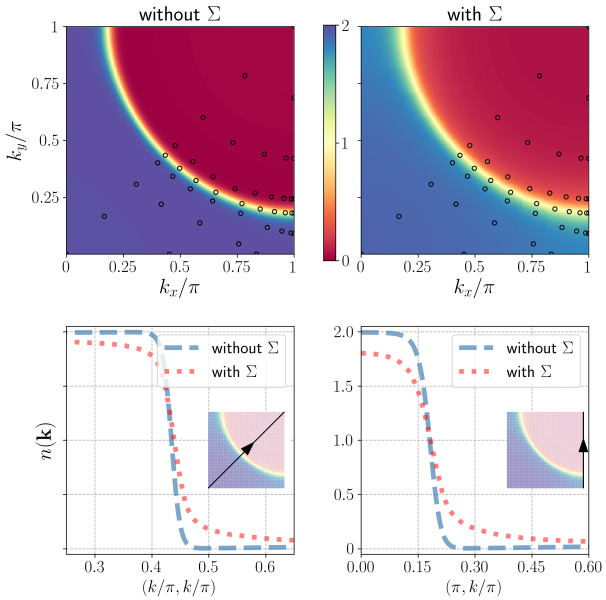

Figure 5: Top row: momentum resolved occupation for $U = 4t$, $t' = -0.32t$, $T = 0.08t$ and doping $x = 0.025$. Left panel non-interacting case. Right panel interacting case. The black circles mark the points used to patch the self-energy. Bottom row: cut of the occupation along the Brillouin zone paths reported as arrows in the insets. Blue dashed curves are without self-energy, while red dotted curves are with self energy.

can see that the enhancement of $\mathcal{M}$ due to self-energy is specific of the large doping region, while, in the small doping region the self energy decreases $\mathcal{M}$. Hence the self-energy affects the magnetic channel either directly by reducing the particle-hole bubble (for small doping), or indirectly through the feedback of other channels, i.e., reducing the charge channel (for large doping).

To understand better these effects we looked for possible changes in the Fermi surface structure, analyzing the momentum distribution, computed as:

$$n(\mathbf{k}) = \frac{2}{\beta} \sum_{\nu} \frac{e^{i\nu 0^+}}{i\nu - \varepsilon_{\mathbf{k}} + \mu^\Lambda - \Lambda\Sigma^\Lambda(\mathbf{k}, i\nu)}. \tag{34}$$

Here the factor 2 accounts for the spin degree of freedom. In Fig. 5 we show the non interacting (top left) and interacting (top right) occupation in the first quadrant of the Brillouin zone for doping $x = 0.025$. The former is computed by setting $\Sigma^\Lambda = 0$ (and non interacting chemical potential) in Eq.(33), while the latter is computed at the critical scale Λ_c.

Comparing the two panels, one does not observe any relevant shift of the Fermi surface position, but the Fermi surface broadening is appreciably larger in the interacting case, due to self-energy. Similar results apply for doping $x = 0.4$, as one can see from Fig. 6, where the broadening

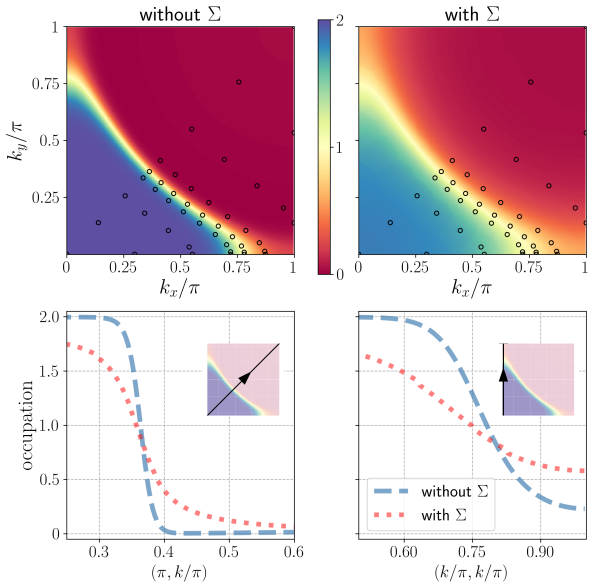

Figure 6: Top row: momentum resolved occupation for $U = 4t$, $t' = -0.32t$, $T = 0.08t$ and doping $x = 0.4$. Left panel non-interacting case. Right panel interacting case. The black circles mark the points used to patch the self-energy. Bottom row: cut of the occupation along the Brillouin zone paths reported as arrows in the insets. Blue dashed curves are without self-energy, while red dotted curves are with self energy.

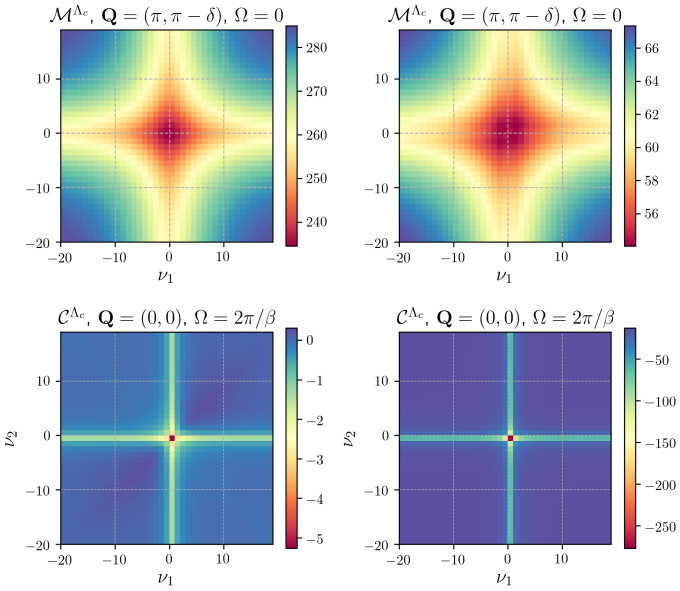

Figure 7: *Top left*: Frequency dependence of the magnetic channel $\mathcal{M}^{\Lambda}_{\Omega,\mathbf{Q}}(\nu_1, \nu_2)$ for $x = 0.025$, $t' = -0.32$, $U = 4t$ and $T = 0.08t$, with self-energy feedback and at the instability vector, and vanishing frequency transfer. *Top right*: Frequency dependence of the magnetic channel $\mathcal{M}^{\Lambda}_{\Omega,\mathbf{Q}}(\nu_1, \nu_2)$ for $x = 0.4$, $t' = -0.32$, $U = 4t$ and $T = 0.08t$, without self-energy feedback and for $\mathbf{Q} = (\pi, \pi - \delta)$, $\delta = 1.13$ (corresponding to the largest magnetic coupling) and for vanishing frequency transfer. *Bottom left*: Frequency dependence of the charge channel $\mathcal{C}^{\Lambda}_{\Omega,\mathbf{Q}}(\nu_1, \nu_2)$ for $x = 0.025$, $t' = -0.32$, $U = 4t$ and $T = 0.08t$, with self-energy feedback and at $\mathbf{Q} = (0, 0)$. The frequency transfer shown is $\Omega = 2\pi T$. *Bottom right*: Frequency dependence of the charge channel $\mathcal{C}^{\Lambda}_{\Omega,\mathbf{Q}}(\nu_1, \nu_2)$ for $x = 0.4$, $t' = -0.32$, $U = 4t$ and $T = 0.08t$, without self-energy feedback and for $\mathbf{Q} = (0, 0)$. The frequency transfer shown is $\Omega = 2\pi T$.

is more evident.

B. Vertex frequency dependence

We now focus on the frequency dependence of the channels. In particular, we will look at the channels that show a divergence, i.e., the charge and the magnetic instabilities observed in Fig. 2, while we refer to the Appendix for the superconducting ones.

As mentioned in the previous section the divergences of the charge and magnetic channels are different. The charge channel diverges for a finite frequency transfer, and only when we neglect the self-energy feedback.

While the dependence on the transfer momentum and frequency $(\mathbf{Q}, \Omega)$ has already been studied elsewhere, e.g., in Ref 1, here we focus on the dependence on the fermionic frequencies. Therefore we present different color plots for fixed $(\mathbf{Q}, \Omega)$, showing the dependence on ν_1 and ν_2.

In the top left panel of Fig. 7 we show the magnetic channel $\mathcal{M}^{\Lambda_c}_{\mathbf{Q}\Omega}(\nu_1, \nu_2)$ in the small doping region, where antiferromagnetism is the leading instability. The case shown has been calculated with self-energy feedback, but the frequency structures we discuss do not depend strongly on the presence of self-energy. For clarity we restrict the plots to the first 20 positive and negative Matsubara frequencies, larger frequencies can be deduced by the asymptotic.[13] When only one channel in Eq. (8) is taken into account, the fRG equations are equivalent to RPA . The magnetic channel calculated with RPA would depend only on the frequency and momentum transfer, that would result, for the plot shown, in a completely constant color. Hence any variation in the frequency structure has to be ascribed to the presence of the other channels in the fRG. As already observed in the literature (WM:who should we cite?), the channel competition suppresses the magnetic channel. This is clear in two ways: the largest value of $\mathcal{M}$ is decreased compared to RPA, and the frequency structure at the center is smaller compared to the asymptotic values.

In the bottom left panel of Fig. 7 we show the charge channel $\mathcal{C}^{\Lambda_c}_{\mathbf{Q},\Omega}(\nu_1, \nu_2)$ for finite frequency transfer $\Omega =$

$2\pi/\beta$, important for the forward scattering instability. The frequency structure is completely different from the case described above. The channel assumes negative values, and the maximum is for frequencies $\nu_1 = \pi/\beta$ and $\nu_2 = -\pi/\beta$. This structure cannot be explained in terms of standard ladder diagrams, and might be also related to the behavior of the retarded interaction described by Ref. 20.

In the two right panels of Fig. 7 we show the same quantities but for $x = 0.4$, without self-energy feedback, for which the charge channel has the largest absolute value. The position of the frequency structures are similar to the one described above. In this case the leading interaction is the localized peak in the charge channel.

Origin of forward scattering To gain insight in the origin of the singular frequency structures observed in the charge channel, we identify a simple set of diagrams reproducing the same features. The idea is that the magnetic channel, which is generated first, is responsible for the increase of the charge channel.

To check this qualitatively, we first compute the magnetic channel by means of RPA; then we use the interaction generated this way in a subsequent RPA equation for the charge channel. Of course one does not expect quantitative agreement with the fRG, since we overestimate both interactions, but the approximation is sufficient to reproduce and explain the qualitative features we are interested in.

We start by introducing a local effective interaction that includes the magnetic fluctuations as computed by RPA[10] in the particle-hole crossed channel:

$$U_{\text{eff},\Omega} = \int_{\mathbf{Q}} \frac{U}{1 - U\Pi_{\mathbf{Q},\Omega}}. \tag{35}$$

Since the bare interaction U is local, U_{eff} depends only on the exchange frequency Ω of the *particle-hole* bubble:

$$\Pi_{\mathbf{Q},\Omega} = \frac{1}{\beta}\sum_{\nu} \Pi_{\mathbf{Q},\Omega}(\nu) = \frac{1}{\beta}\sum_{\nu}\int_{\mathbf{p}} G_{0,\mathbf{p},\nu} G_{0,\mathbf{p}+\mathbf{Q},\nu+\Omega}. \tag{36}$$

Here we introduced also the ν-dependent bubble $\Pi_{\mathbf{Q},\Omega}(\nu)$, since, as we will see, it plays a special role in the origin of the charge divergences.

The magnetic effective interaction in Eq. (34) will be now used to compute the RPA equation for the charge channel:

$$\mathcal{C}_{\mathbf{Q},\Omega}(\nu_1,\nu_3) = U_{\text{eff},\nu_1-\nu_3}\left[\delta_{\nu_1,\nu_3} + U_{\text{eff},\nu_1-\nu_3}\Pi_{\mathbf{Q},\Omega}(\nu_1)\right]^{-1}. \tag{37}$$

Here the charge channel is expressed in terms of ν_1 and $\nu_3 = \nu_2 - \Omega$ rather than in terms of ν_1 and ν_2. Eq. (36) is nothing more than an RPA equation with a frequency dependent interaction in the particle-hole channel.[10] U_{eff} depends on $\nu_1 - \nu_3$ due to the frequency exchange from particle-hole crossed to particle-hole notation. We note that, in the case of a frequency independent effective interaction U_{eff}, Eq.(36) becomes ν_1 and ν_3 independent and only the summed bubble $\Pi_{\mathbf{Q},\Omega}$ appears. The frequency dependence of U_{eff} qualitatively affects the results.

In Fig. 8, we show the charge channel as computed by Eq. (36) for different Ω, $\mathbf{Q} = (0,0)$ as a function of ν_1 and ν_2, for $T = t$, $t' = -0.32t$, $U = 4t$ and $x = 0.375$. We consider such a high temperature due to the above-mentioned overestimation of the fluctuations within RPA. The frequency structure in Fig. 8 for $\Omega = 2\pi/\beta$ is very similar to the one shown in Fig. 7. The simple diagrams considered here reproduce the position of the main structures, as well as the correct sign of the charge channel. This is true also for the other bosonic Matsubara frequency shown here, for which we do not report the fRG results. Furthermore, upon lowering the temperature the charge channel diverges also for other finite bosonic Matsubara frequencies, while it does not diverge for $\Omega = 0$. From this we conclude that the diagrams described here are responsible for the frequency structure of the charge channel observed in fRG.

To understand why the divergence appears for a finite frequency Ω, we notice that in Eq.(36) the Ω dependence appears only through the bubble $\Pi_{\mathbf{Q},\Omega}(\nu)$. The frequency summed particle-hole bubble obeys the following relation:

$$\Pi_{\mathbf{Q}\to(0,0),\Omega} = \frac{1}{\beta}\sum_{\nu}\Pi_{\mathbf{Q}\to(0,0),\Omega}(\nu) = C\delta_{\Omega,0}, \tag{38}$$

where C is a constant that, at low temperature, approaches the density of states at the Fermi level. In the rightmost panel of Fig. 8, we show the bubble $\Pi_{\mathbf{Q}=(0,0),\Omega}(\nu)$ as a function of ν for different values of Ω. We note that it has a large negative peak for $\Omega = 2\pi/\beta$. This is due to the property (37): the summed bubble must vanish for $\Omega \neq 0$, hence a large negative value is needed to cancel the positive contributions at large frequency. We have thus identified the origin of the frequency structure observed in the charge channel, which seems to be quite general and arising from simple diagrams.

Including the self-energy in the calculation of the bubble, Eq. (37) does not evaluate to a δ-function anymore, and the difference between the summed bubble at vanishing frequency and for frequency $2\pi T$ is diminished. This is probably the reason why the inclusion of the self-energy feedback is sufficient to avoid the divergence of the charge channel.

C. Self energy analysis

We discuss here the frequency and momentum dependence of the self energy. In Fig. 9 we show the frequency dependence of the imaginary part of the self-energy for $U = 4t$, $T = 0.08t$, $t' = -0.32t$ and doping $x = 0.025$.

This spread between the maximal and minimal self-energy at each frequency is rather small, indicating that

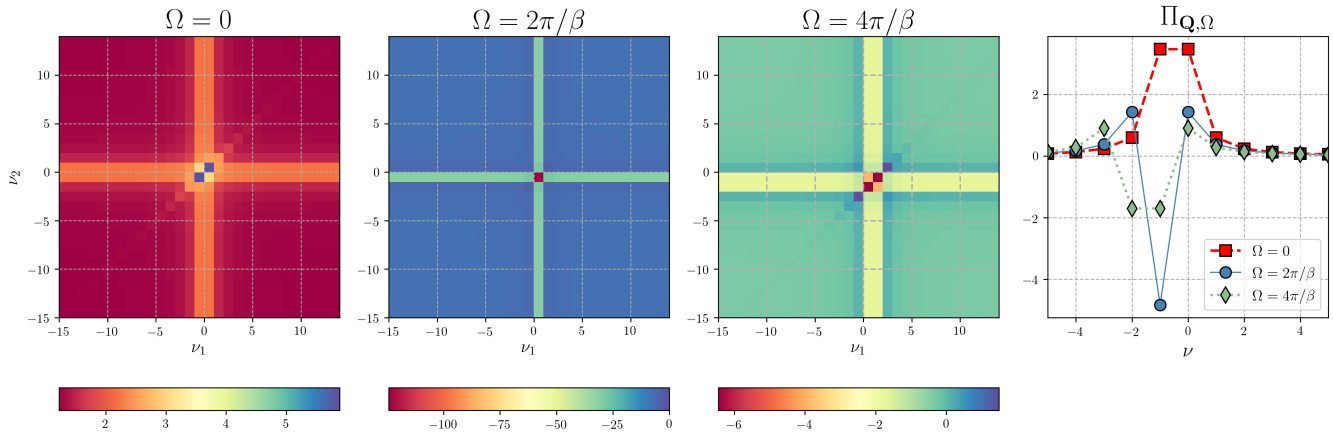

Figure 8: In the first three panels from the left, the charge channel $\mathcal{C}_{\mathbf{Q},\Omega}$ as in Eq. 36 is shown as a function of ν_1 and ν_2 for frequency $\Omega = 0$, $\Omega = 2\pi/\beta$ and $\Omega = 4\pi/\beta$, respectively, for $\mathbf{Q} = (0, 0)$. In the most right panel, the bubble $\Pi_{\mathbf{Q}=(0,0),\Omega}(\nu)$ is shown as a function of ν for $\Omega = 0$, $\Omega = 2\pi/\beta$ and $\Omega = 4\pi/\beta$. All plots refer to parameters $T = 1.0$, $t' = -0.32$, $x = 0.375$ and $U = 4$.

the self-energy did not develop a large momentum dependence even when the vertex reached the critical scale. For all the momenta, the self-energy shows a Fermi-liquid like behavior (at finite temperature). In this situation one would expect the antinodal region to be more affected by correlation effects. However, we can only see a slight increase of the (absolute value of) self energy in this region. At the temperature that we are considering, we do not observe a tendency towards the opening of a momentum selective gap.

In Fig. 10 we show the imaginary part of the self-energy for a larger doping $x = 0.400$. For these parameters the incommensurability reaches its maximal value $\delta = 1.13$. As in the previous case, we do not see much momentum differentiation.

The self-energy enters directly in the calculation of the momentum resolved occupation through the Green's function, already discussed above, and shown in Figs. 5 and 6. In the bottom panels of these figures, we show how the occupation evolves along two different cuts in the Brillouin zone. The two cuts are shown by arrows in the inset, and cross, respectively, the *nodal* and *antinodal* regions. The occupation drop is sharper along the main diagonal, and the self-energy affects more the occupation along the nodal cut. For doping $x = 0.4$ the broadening of the Fermi surface, already larger at the non interacting level, is further enhanced by the self-energy.

To study further the difference between nodal and antinodal regions in the iAF case, we studied the quasiparticle weight[3,21] $\mathcal{Z}_{\mathbf{k}}$, and the decay rate $\gamma_{\mathbf{k}}$. Instead of relying on analytical continuation, we have extracted the parameters directly from the imaginary axis data. To do so we have fitted the first few frequencies of the imaginary part of the self-energy with a polynomial of degree l: $\mathrm{Im}\Sigma(\mathbf{k}, i\nu) \approx a_0(\mathbf{k}) + a_1(\mathbf{k})\nu + ... + a_l(\mathbf{k})\nu^l$ and we identified $\gamma_{\mathbf{k}} = a_0(\mathbf{k})$, $\mathcal{Z}_{\mathbf{k}} = \frac{1}{1-a_1(\mathbf{k})}$. The procedure only works if the temperature is small enough, and if the frequencies used for the fitting are not too high. We checked that the results were stable by changing the number of frequencies and the order of the polynomial used for the fit. The results are shown in Fig. 11, where the value of $\mathcal{Z}_{\mathbf{k}}$ and $\gamma_{\mathbf{k}}$ is plotted against the angle θ along the Fermi surface, $\theta = 0$ corresponding to the antinodal point and $\theta = \pi/4$ to the nodal one. The variation of the quasiparticle weight along the Fermi surface is extremely small with $\mathcal{Z}$ assuming values between 0.754 and 0.760. On the other hand the relative variation of the decay rate γ along the Fermi surface is larger, varying from $\gamma \approx 0.056t$ and $\gamma \approx 0.082t$. These values are comparable with the temperature $T = 0.08t$. We conclude that at the critical scale, the system still has coherent quasiparticles along all the Fermi surface, with a higher decay rate in the antinodal region. This is consistent with the observations of Ref.[22], where it is shown that non Fermi liquid behavior of the self-energy is observed only very close to the critical temperature and in the immediate vicinity of the hot spots. *I did not really know where to add the citation, we can expand commenting that it is Wick-ordered?*

V. CONCLUSIONS

- order of the paragraph? shall we discuss first self energy or vertex?

- do we want to show more vertex structure in the appendix?

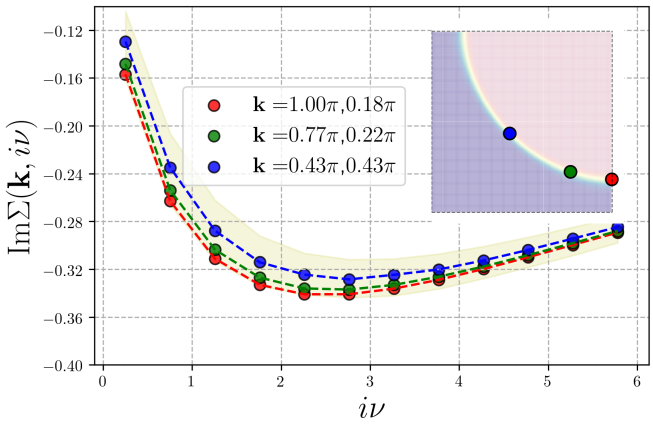

Figure 9: Frequency dependent self-energy for $U = 4t$, $T = 0.08t$, $t' = -0.32t$, $x = 0.025$. Red symbols refer to the Fermi surface momentum in the antinodal direction, blue symbols to the Fermi surface momentum on the diagonal, while green symbols refer to a momentum on the Fermi-surface between these two extremes. The location of the $\mathbf{k}$-point in the Brillouin zone is color coded in the inset. The position of all the patching points taken into account for the self-energy is shown as black circles in the top row of Figs. 5 and 6, and does not change during the flow. The shaded area highlights the region between the maximal and minimal value of the self-energy for each frequency.

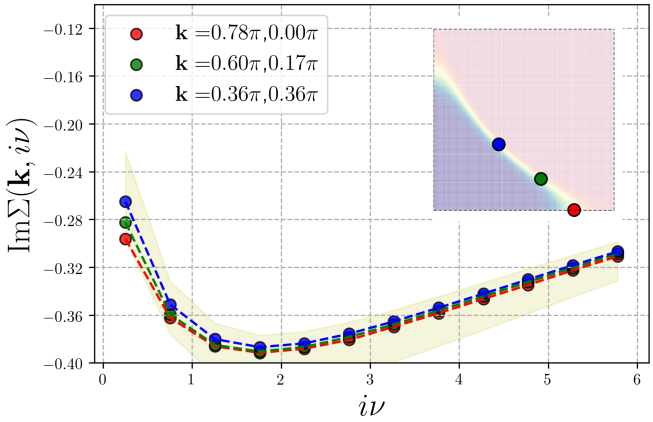

Figure 10: Frequency dependent self-energy for $U = 4t$, $T = 0.08t$, $t' = -0.32t$, $x = 0.4$. Red symbols refer to the Fermi surface momentum in the antinodal direction, blue symbols to the Fermi surface momentum on the diagonal, while green symbols refer to a momentum on the Fermi-surface between these two extremes. The location of the $\mathbf{k}$-point in the Brillouin zone is color coded in the inset. The position of all the patching points taken into account for the self-energy is shown as black circles in the top row of Figs. 5 and 6, and does not change during the flow. The shaded area is the region between the maximal and minimal value of the self-energy for each frequency.

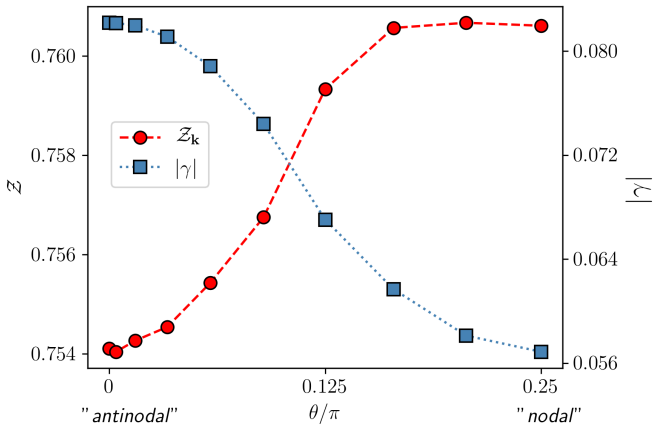

Figure 11: Quasiparticle weight $\mathcal{Z}_\mathbf{k}$ and decay rate $\gamma_\mathbf{k}$ as function of the angle θ. The values on the left axis refer to the quasiparticle weight. The values on the right axis refer to the decay rate.

Acknowledgments

We thank for valuable discussions .... This research was supported by.

VI. APPENDICES

A. Flow equations

We here report the final expression for the flow equations of each channel. To simplify the notation from now on we omit the Λ dependencies. The flow equation for the s-wave superconductivity channel $\mathcal{S}$ reads:

$$\dot{\mathcal{S}}_{\mathbf{Q}}^{\Omega;\nu_1,\nu_3} = \frac{1}{2}\sum_{\nu} L_{\mathrm{s}\mathbf{Q}}^{\Omega;\nu_1,\nu} P_{\mathrm{s},\mathbf{Q}}^{\Omega,\nu} L_{\mathrm{s}\mathbf{Q}}^{\Omega;\nu,\Omega-\nu_3} + \frac{1}{2}\sum_{\nu} L_{\mathrm{s}\mathbf{Q}}^{\Omega;\Omega-\nu_1,\nu} P_{\mathrm{s},\mathbf{Q}}^{\Omega,\nu} L_{\mathrm{s}\mathbf{Q}}^{\Omega;\nu,\nu_3}, \tag{39}$$

with:

$$P_{\mathrm{s},\mathbf{Q}}^{\Omega;\omega} = \int_{\mathbf{p}} G_{\mathbf{p},\omega} S_{\mathbf{Q}-\mathbf{p},\Omega-\omega} + G_{\mathbf{Q}-\mathbf{p},\Omega-\omega} S_{\mathbf{p},\omega}, \tag{40}$$

and:

$$L_{\mathrm{s}\mathbf{Q}}^{\Omega;\nu_1,\nu_3} = U - \mathcal{S}_{\mathbf{Q}}^{\Omega;\nu_1,\nu_3} + \int_{\mathbf{p}} \Big[\mathcal{M}_{\mathbf{p}}^{\nu_3-\nu_1;\nu_1,\Omega-\nu_1} + \frac{1}{2}\mathcal{M}_{\mathbf{p}}^{\Omega-\nu_1-\nu_3;\nu_1,\Omega-\nu_1} - \frac{1}{2}\mathcal{C}_{\mathbf{p}}^{\Omega-\nu_1-\nu_3;\nu_1,\Omega-\nu_1}\Big]. \tag{41}$$

The flow equation for the d-wave superconductivity channel $\mathcal{D}$ reads:

$$\dot{\mathcal{D}}_{\mathbf{Q}}^{\Omega;\nu_1,\nu_3} = \frac{1}{2}\sum_{\nu} L_{\mathrm{d}\mathbf{Q}}^{\Omega;\nu_1,\nu} P_{\mathrm{d},\mathbf{Q}}^{\Omega,\nu} L_{\mathrm{d}\mathbf{Q}}^{\Omega;\nu,\Omega-\nu_3} + \frac{1}{2}\sum_{\nu} L_{\mathrm{d}\mathbf{Q}}^{\Omega;\Omega-\nu_1,\nu} P_{\mathrm{d},\mathbf{Q}}^{\Omega,\nu} L_{\mathrm{d}\mathbf{Q}}^{\Omega;\nu,\nu_3}, \tag{42}$$

with:

$$P_{\mathrm{d},\mathbf{Q}}^{\Omega;\omega} = \int_{\mathbf{p}} f_{\mathrm{d}}\left(\frac{\mathbf{Q}}{2}-\mathbf{p}\right)^2 \left[G_{\mathbf{p},\omega} S_{\mathbf{Q}-\mathbf{p},\Omega-\omega} + G_{\mathbf{Q}-\mathbf{p},\Omega-\omega} S_{\mathbf{p},\omega}\right], \tag{43}$$

and:

$$L_{\mathrm{d}\mathbf{Q}}^{\Omega;\nu_1,\nu_3} = -\mathcal{D}_{\mathbf{Q}}^{\Omega;\nu_1,\nu_3} + \frac{1}{2}\int_{\mathbf{p}} (\cos p_x + \cos p_y)\Big[\mathcal{M}_{\mathbf{p}}^{\nu_3-\nu_1;\nu_1,\Omega-\nu_1} + \frac{1}{2}\mathcal{M}_{\mathbf{p}}^{\Omega-\nu_1-\nu_3;\nu_1,\Omega-\nu_1} - \frac{1}{2}\mathcal{C}_{\mathbf{p}}^{\Omega-\nu_1-\nu_3;\nu_1,\Omega-\nu_1}\Big]. \tag{44}$$

Since $\mathcal{D}$ is generated during the flow by the other channels only, see Eq. (43), it is the most sensitive channel to the frequency approximation made. Neglecting the vertex frequency one will likely overestimate L_{d}, as already mentioned in Ref. 1.

The flow equation for the charge channel $\mathcal{C}$ reads:

$$\dot{\mathcal{C}}_{\mathbf{Q}}^{\Omega;\nu_1,\nu_2} = \sum_{\nu} L_{\mathrm{c}\mathbf{Q}}^{\Omega;\nu_1,\nu} P_{\mathbf{Q}}^{\Omega,\nu} L_{\mathrm{c}\mathbf{Q}}^{\Omega;\nu,\nu_2-\Omega}, \tag{45}$$

with:

$$L_{\mathrm{c}\mathbf{Q}}^{\Omega;\nu_1,\nu_2} = U - \mathcal{C}_{\mathbf{Q}}^{\Omega;\nu_1,\nu_2} + \int_{\mathbf{p}} \Big[-2\mathcal{S}_{\mathbf{p}}^{\nu_1+\nu_2;\nu_1,\nu_2-\Omega} + \mathcal{S}_{\mathbf{p}}^{\nu_1+\nu_2;\nu_1,\Omega+\nu_1} \tag{46}$$

$$+ \left(\mathcal{D}_{\mathbf{p}}^{\nu_1+\nu_2;\nu_1,\nu_2-\Omega} - \frac{1}{2}\mathcal{D}_{\mathbf{p}}^{\nu_1+\nu_2;\nu_1,\Omega+\nu_1}\right)\left[\cos(Q_x)+\cos(Q_y)\right] \tag{47}$$

$$+ \frac{3}{2}\mathcal{M}_{\mathbf{p}}^{\nu_2-\nu_1-\Omega;\nu_1,\nu_2} + \frac{1}{2}\mathcal{C}_{\mathbf{p}}^{\nu_2-\nu_1-\Omega;\nu_1,\nu_2}\Big], \tag{48}$$

while $P_{\mathbf{Q}}^{\Omega;\omega}$ is given in Eq. (27). The equation for the magnetic channel is reported in Eq. (26). The form factor decomposition allows to decouple the momentum integrals, in the calculation of the L's, Eqns. (28), (40), (43) and (45), from the frequency summations in the flow equations, hence reducing the numeric effort.

[1] C. Husemann, K.-U. Giering, and M. Salmhofer. Frequency-dependent vertex functions of the (t, t') hubbard model at weak coupling. *Phys. Rev. B*, 85:075121,

Feb 2012.

[2] J. Hubbard. Electron Correlations in Narrow Energy Bands. *Proc. R. Soc. A*, 276:238–257, November 1963.

[3] W. Metzner, M. Salmhofer, C. Honerkamp, V. Meden, and K. Schönhammer. Functional renormalization group approach to correlated fermion systems. *Rev. Mod. Phys.*, 84:299–352, January 2012.

[4] C. Platt, W. Hanke, and R. Thomale. Functional renormalization group for multi-orbital fermi surface instabilities. *Advances in Physics*, 62(4-6):453–562, 2013.

[5] C. Wetterich. Exact evolution equation for the effective potential. *Physics Letters B*, 301:90–94, February 1993.

[6] M. Salmhofer and C. Honerkamp. Fermionic Renormalization Group Flows —Technique and Theory—. *Prog. Theor. Phys.*, 105:1–35, January 2001.

[7] Binz, B., Baeriswyl, D., and DouÃğot, B. Wilson's renormalization group applied to 2d lattice electrons in the presence of van hove singularities. *Eur. Phys. J. B*, 25(1):69–87, 2002.

[8] B. Binz, D. Baeriswyl, and B. DouÃğot. Weakly interacting electrons and the renormalization group. *Annalen der Physik*, 12(11-12):704–736, 2003.

[9] F. B. Kugler and J. von Delft. Multiloop functional renormalization group that sums up all parquet diagrams. *ArXiv e-prints*, March 2017.

[10] G. Rohringer, A. Valli, and A. Toschi. Local electronic correlation at the two-particle level. *Phys. Rev. B*, 86(12):125114, September 2012.

[11] C. Husemann and M. Salmhofer. Efficient parametrization of the vertex function, Ω scheme, and the t,t′ Hubbard model at van Hove filling. *Phys. Rev. B*, 79(19):195125, May 2009.

[12] J. Lichtenstein, D. SÃąnchez de la PeÃśa, D. Rohe, E. Di Napoli, C. Honerkamp, and S.A. Maier. High-performance functional renormalization group calculations for interacting fermions. *Computer Physics Communications*, 213:100 – 110, 2017.

[13] N. Wentzell, G. Li, A. Tagliavini, C. Taranto, G. Rohringer, K. Held, A. Toschi, and S. Andergassen. High-frequency asymptotics of the vertex function: diagrammatic parametrization and algorithmic implementation. *ArXiv e-prints*, October 2016.

[14] C. Karrasch, R. Hedden, R. Peters, T. Pruschke, K. Schönhammer, and V. Meden. A finite-frequency functional renormalization group approach to the single impurity Anderson model. *J. Phys.: Condens. Matter*, 20:H5205, August 2008.

[15] C. Taranto, S. Andergassen, J. Bauer, K. Held, A. Katanin, W. Metzner, G. Rohringer, and A. Toschi. From Infinite to Two Dimensions through the Functional Renormalization Group. *Phys. Rev. Lett.*, 112(19):196402, May 2014.

[16] C. Honerkamp, D. Rohe, S. Andergassen, and T. Enss. Interaction flow method for many-fermion systems. *Phys. Rev. B*, 70(23):235115, December 2004.

[17] Nils Wentzell, Serge Florens, Tobias Meng, Volker Meden, and Sabine Andergassen. Magneto-electric spectroscopy of andreev bound states in josephson quantum dots. May 2016.

[18] A. Eberlein. Fermionic two-loop functional renormalization group for correlated fermions: Method and application to the attractive Hubbard model. *Phys. Rev. B*, 90(11):115125, September 2014.

[19] N. D. Mermin and H. Wagner. Absence of ferromagnetism or antiferromagnetism in one- or two-dimensional isotropic heisenberg models. *Phys. Rev. Lett.*, 17:1133–1136, Nov 1966.

[20] E. A. Stepanov, E. G. C. P. van Loon, A. A. Katanin, A. I. Lichtenstein, M. I. Katsnelson, and A. N. Rubtsov. Self-consistent dual boson approach to single-particle and collective excitations in correlated systems. *Phys. Rev. B*, 93:045107, Jan 2016.

[21] A.A. Abrikosov, L.P. Gorkov, and Dzyaloshinski I.E. *Methods of quantum field theory in statistical physics.* 1963.

[22] Daniel Rohe and Walter Metzner. Pseudogap at hot spots in the two-dimensional hubbard model at weak coupling. *Phys. Rev. B*, 71:115116, Mar 2005.

[23] The equation for the particle-particle channel is slightly different from the one usually reported in fRG, see, e.g., Ref. 11. This is because we took $V^\Lambda = V^\Lambda_{\uparrow\downarrow\uparrow\downarrow}$ instead of $V^\Lambda = V^\Lambda_{\uparrow\downarrow\downarrow\uparrow}$.